Dalton Transactions



PAPER

View Article Online



Cite this: *Dalton Trans.*, 2021, **50**, 2149

Back donation, intramolecular electron transfer and N-O bond scission targeting nitrogen oxyanion reduction: how can a metal complex assist?†

Daniel M. Beagan, ‡ Alyssa C. Cabelof ‡ and Kenneth G. Caulton • *

A density functional theory exploration studies a range of ancillary coordinated ligands accompanying nitrogen oxyanions with the goal of promoting back donation towards varied nitrogen oxidation states. Evaluation of a suite of Ru and Rh metal complexes reveals minimum back donation to the κ^1 -nitrogen oxyanion ligand, even upon one-electron reduction. This reveals some surprising consequences of reduction, including redox activity at pyridine and nitrogen oxyanion dissociation. Bidentate nitrate was therefore considered, where ancillary ligands enforce geometries that maximize $M-NO_X$ orbital overlap. This strategy is successful and leads to full electron transfer in several cases to form a pyramidal radical NO_3^{2-} ligand. The impact of ancillary ligand on degree of nitrate reduction is probed by comparing the powerful o-donor tris-carbene borate (TCB) to a milder donor, tris-pyrazolyl borate (Tp). This reveals that with the milder Tp donor, nitrate reduction is only seen upon addition of a Lewis base. Protonation of neutral and anionic (TCB)Ru(κ^2-NO_3) at both terminal and internal oxygens reveals exergonic N-O bond cleavage for the reduced species, with one electron coming from Ru, yielding a Ru^{III} hydroxide product. Comparison of H⁺ to Na^+ electrophile shows weaker progress towards N-O bond scission. Finally, calculations on (TCB)Fe(κ^2-NO_3) and [(TCB)Fe(κ^2-NO_3)] show that electron transfer to nitrate is possible even with an earth abundant 3d metal.

Received 5th October 2020, Accepted 11th January 2021 DOI: 10.1039/d0dt03430d

Introduction

rsc li/dalton

Nitrate reduction and nitrogen oxyanion reduction in general has garnered much attention recently owing to the environmental impact of these oxyanions in bodies of water, causing eutrophication and dead zones. The reduction of nitrogen oxyanions has been achieved through a variety of approaches, spanning electrochemical, hotochemical, and chemical reagent pathways. The first step in nitrate reduction is the two electron process transforming $\rm NO_3^-$ to $\rm NO_2^-$, which involves the breaking of an N-O bond. This is mirrored by subsequent reductions, all of which require cleavage of increasingly strong bonds.

We anticipate that routes to weaken the N–O bonds will make reductive processes more facile, and a previously unexplored possibility is to utilize the fact that the LUMO of nitrate and nitrite are π_{NO}^* in character (Fig. 1), and are therefore

Department of Chemistry, Indiana University, 800 E. Kirkwood Ave., Bloomington, IN. 47401. USA. E-mail: caulton@indiana.edu

‡These authors contributed equally to this work.

somewhat analogous to well-known π -acceptors (cyanide, carbene, silylene). The antibonding character of these LUMOs shows that population will weaken all N–O bonds, and therefore any back donation has the potential for bond weakening. We seek to answer the following questions: (1) What metal oxidation states favor π donation from metal to ligand? (2) Does valence electron count affect π donation? (3) Does NO₃⁻ denticity affect degree of π donation? (4) What ancillary ligand features increase such π donation? (5) As back donation is

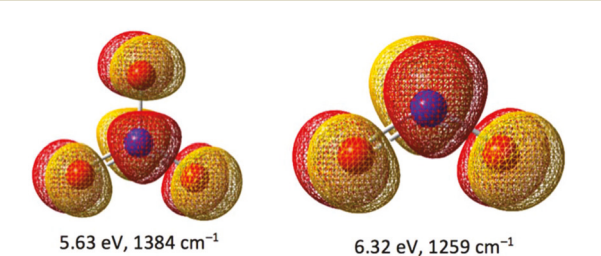


Fig. 1 LUMO of nitrate (left) and LUMO of nitrite (right) with respective LUMO energies and N-O stretching frequencies. The LUMO of nitrate lies 0.69 eV lower than that of nitrite, yielding a smaller energy gap from the d orbital which might back donate.

 $[\]dagger$ Electronic supplementary information (ESI) available: Structural analysis and . mol files of each optimized structure. See DOI: 10.1039/d0dt03430d

increased and oxygen becomes more electron rich, to what extent will attachment of an electrophile enhance π donation and weaken an N-O bond targeted for cleavage? More generally, we are also interested in learning about the geometric and electronic structure of species relevant to NO_x^- deoxygenation.

All of the above questions specific to nitrate are equally pertinent for the next step in deoxygenation, that of coordinated NO₂⁻, and will be analyzed here for isomeric nitro and nitrito binding modes. This is a heavy burden of questions to ask experimentally, and Density Functional Theory calculations are reliable enough to identify the trends we seek to uncover. Therefore, we use this approach to identify specific design principles for discovering complexes suited to facilitate NO_x deoxygenation. We will employ a variety of observables calculated with DFT in addition to orbital analyses to strengthen any detected trends.

Results

We employed DFT calculations at the B3LYP-D3BJ/6-311G(d,p) level of theory in all results reported here. Our initial suite of test compounds began with CpRu(PMe₃)(L)(X) (L and X ligands defined in Fig. 2) with comparative calculations on Rh (PMe₃)₂(L)(X). This allowed us to probe the effects of moving from 18 to 16 valence electron species, and the influence of pseudo octahedral vs. planar geometry on the potential π -acidity of nitrate. Additionally, we incorporate a CO ligand to give a gauge of back donation via calculated CO stretching frequencies. We compared these to analogous pyridine complexes, anticipating a change in the corresponding X ligand stretching frequency due to increased electron density at the metal center as CO is replaced by pyridine. The neutral and mono-anionic (1 electron reduced) complexes were computed for each species shown in Fig. 2 to assess the effect of reduction on potential electron density leakage onto the NO_x ligand.

These compounds gave conflicting evidence about the ability of nitrate to act as a π acid. While the stretching frequencies in some cases suggested that nitrate was in fact the best π acid, bond length analyses and a lack of spin density leakage onto the NO_x ligand in the radical anion complexes contradicted the computed IR data. A detailed description of these results is included in the ESI.† We attribute the spectroscopic discrepancy to two factors. The first is due to competing

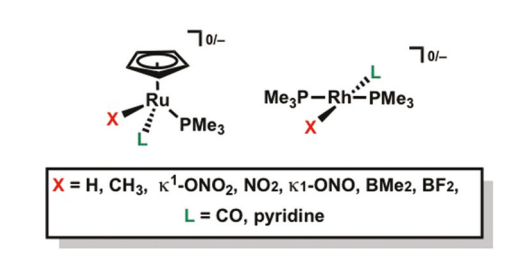


Fig. 2 Various ruthenium and rhodium complexes studied

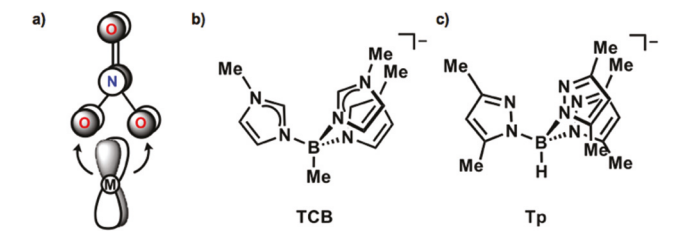


Fig. 3 (a) Orbital overlap for a metal d-orbital with bidentate nitrate π^* (b) C_{3V} symmetric tris-carbene borate (TCB) and (c) tris-pyrazolyl borate (Tp) ligands used in this study.

 σ and π effects of our X ligand in our test set. The second is the lack of good orbital overlap between monodentate NO_x and the metal in these optimized geometries. We hypothesize that there is poor overlap between the π^* orbital of κ^1 -nitrate with any metal $d\pi$ orbital, and our focus therefore shifted to bidentate nitrate for improved orbital overlap (Fig. 3).

Tris-carbene borate ancillary ligand

Nitrate. We chose a strongly σ -donating tris N-heterocyclic carbene (NHC) borate ligand, $^{28-31}$ (TCB, Fig. 3b) to enforce C_{3v} symmetry and allow us to study the effects of bidentate nitrate. We optimized the neutral (TCB)Ru(κ^2 -NO₃) and the one electron reduced species, $[(TCB)Ru(\kappa^2-NO_3)]^-$ to probe whether the added electron populates the $[(TCB)Ru]^+$ unit or the nitrate π^* . Optimization of the neutral (TCB)Ru(κ²-NO₃) species results in a square pyramidal complex (Fig. 4a) with equidistant Ru-O distances of planar nitrate along with two equal Ru-Ccarbene distances comprising the basal plane. The internal N-O distances are equivalent and 0.084 Å longer than the terminal N-O, which is indicative of localized double bond character on

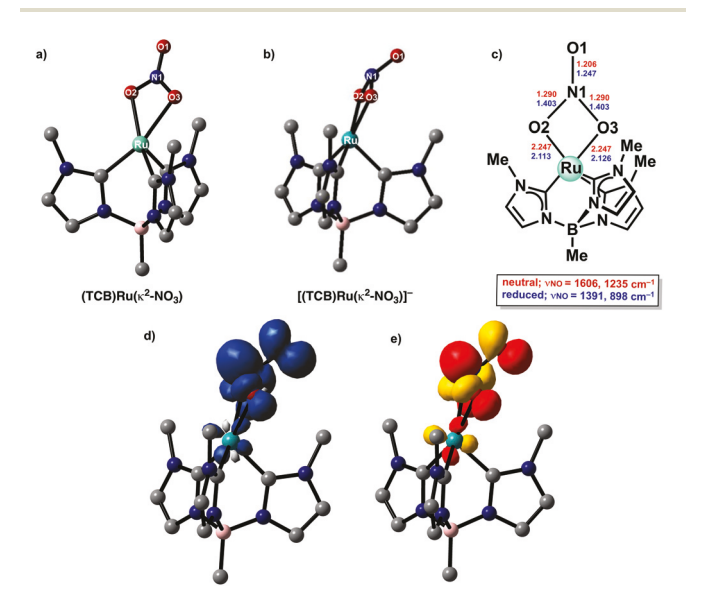


Fig. 4 (a) Optimized structure for (TCB)Ru(κ^2 -NO₃) (b) optimized structure for $[(TCB)Ru(\kappa^2-NO_3)]^-$ (c) relevant bond length comparison and stretching frequencies for the neutral vs. anionic complex (d) spin density plot (0.002 au) of $[(TCB)Ru(\kappa^2-NO_3)]^-$ and (e) SOMO (0.05 au) of $[(TCB)Ru(\kappa^2-NO_3)]^-$.

Dalton Transactions Paper

the terminal N-O, consistent with Fig. 3a. Optimization of the anionic complex, $[(TCB)Ru(\kappa^2-NO_3)]^-$, retains a square pyramidal structure, however, the nitrate nitrogen is pyramidalized (Fig. 4b) with a Ru-N1-O1 angle of 146.4°. The pyramidalization of one-electron reduced nitrate has been previously identified by DFT calculations of the mechanism of electrocatalytic nitrate reduction. 10,32 The radical character on nitrate is confirmed by the spin density plot (Fig. 4d), which shows character primarily on the nitrate π^* . The spin density mirrors the SOMO of $[(TCB)Ru(\kappa^2-NO_3)]^-$ (Fig. 4e). Bond length changes (Fig. 4c) are consistent with population of the nitrate π^* upon reduction, where each Ru-O distance decreases while every N-O bond distance lengthens.

Reduction is accompanied by significant decrease of ν_{NO} from 1606 and 1235 cm⁻¹ in the neutral species to 1391 and 898 cm⁻¹ in the reduced species. This example shows through multiple observables, in addition to spin density plots, that the N-O bonds are indeed weakened in this system via a 1-electron reduction.

Nitrite. For the aforementioned reasons, we were also interested in whether the TCB ligand on Ru could also help accomplish reduction of nitrite, a less oxidized nitrogen. Analogous calculations were done on the 16 valence electron species $(TCB)Ru(\kappa^2-ONO)$ (bidentate nitrite) and $(TCB)Ru(NO_2)$ (monodentate nitro). The bidentate nitrite complex optimizes to a square pyramidal geometry (Fig. 5a) and upon reduction, the spin density, bond lengths, and stretching frequencies are all consistent with population of the nitrite π^* (Fig. 5b-d). The SOMO of $[(TCB)Ru(\kappa^2-ONO)]^-$ (Fig. 5e) shows comparable metal and nitrite character, in contrast to spin localization on nitrate in $[(TCB)Ru(\kappa^2-NO_3)]^-$. This indicates back donation from Ru^{II}, rather than complete electron transfer. In the case

of monodentate nitro, the initially four coordinate (TCB)Ru (NO₂) species optimizes to a see-saw geometry (Fig. 5f). The nitro group is asymmetrically bound with N-O bond distances differing by 0.06 Å and the longer N-O bond having a Ru-N-O bond angle of 90.3°. This asymmetric binding follows from a short Ru-O distance of 2.42 Å, indicating an interaction between ruthenium and oxygen, which is driven by the initially 14 valence electron count of ruthenium. Upon reduction, that Ru-O distance lengthens by 0.12 Å, consistent with a more electron rich metal needing less donation from the pendent oxygen nucleophile. The spin density plot, bond lengths, and N-O stretching frequencies in [(TCB)Ru(NO₂)]⁻ (Fig. 5g-i) are consistent with back donation into nitro π^* upon reduction, but the geometry about the nitro N is planar. Analogous to $[(TCB)Ru(\kappa^2-ONO)]^-$, the SOMO of $[(TCB)Ru(NO_2)]^-$ (Fig. 5j) shows equal contribution from metal and nitro, consistent with strong back donation but not full 1 electron reduction of nitrite.

In summary, the extended π -system of κ^2 -nitrate allows for more efficient redox transfer and therefore upon one-electron reduction, full electron transfer to the nitrate is observed. In contrast, the nitrite radical anion shows reduction at the metal center with a more classical picture of back donation.

The effect of denticity. The calculations on the TCB systems thus far show that bidentate linkage for nitrate and nitrito ligands helps aide in reduction. To test if bidentate NO_x⁻ linkage is essential, we geometry optimized both the four coordinate 14 valence electron (TCB)Ru(κ1-NO3) and (TCB)Ru(κ1-ONO) along with the anions for each. In the case of monodentate nitrate, the neutral and monoanionic complexes are best described as see-saw about the ruthenium center (Fig. S30a†). The spin density plot of $[(TCB)Ru(\kappa^{1}-NO_{3})]^{-}$

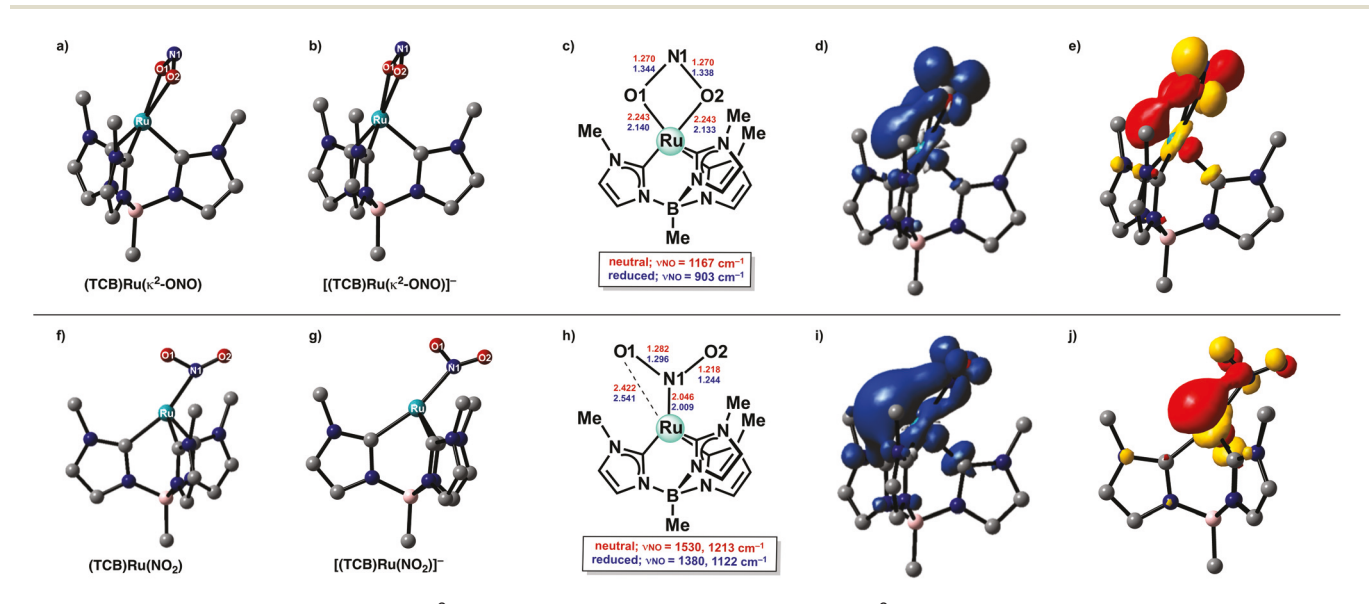


Fig. 5 (a) Optimized structure for (TCB)Ru(κ^2 -ONO) (b) optimized structure for [(TCB)Ru(κ^2 -ONO)] $^-$ (c) relevant bond length comparison and stretching frequencies for the neutral vs. anionic complex with nitrito (d) spin density plot (0.002 au) of [(TCB)Ru(κ^2 -ONO)]⁻ (e) SOMO (0.05 au) of $[(TCB)Ru(\kappa^2-ONO)]^-$ (f) Optimized structure for $(TCB)Ru(NO_2)$ (g) optimized structure for $[(TCB)Ru(NO_2)]^-$ (h) relevant bond length comparison and stretching frequencies for the neutral vs. anionic complex with nitro (i) spin density plot (0.002 au) of [(TCB)Ru(NO₂)]⁻ and (j) SOMO (0.05 au) of $[(TCB)Ru(\kappa^2-NO_2)]^-$.

(Fig. S30b†) has some spin leakage onto the nitrate ligand but the Ru-O distance is lengthened by 0.049 Å, accompanied by a shorter internal N-O bond distance and longer terminal N-O distances (see ESI†). Furthermore, upon reduction, the asymmetric nitrate N-O stretching frequency decreases by only 83 cm⁻¹. These results sharply contrast the result obtained for the bidentate nitrate complex ($\Delta \nu_{NO} = 215 \text{ cm}^{-1}$) and strongly suggest that denticity plays an important role in the population of the nitrate π^* system. Importantly, the bidentate (TCB)Ru(κ²-NO₃) complex is lower in energy than the monodentate isomer by 13.5 kcal mol⁻¹. Higher metal connectivity to nitrate raises the d orbital energies due to an increased ligand field, which encourages charge flow to nitrate. Furthermore, the HOMO through HOMO-3 of the bidentate nitrate complex are each higher in energy than in the monodentate nitrate complex, which facilitates population of nitrate π^* upon reduction.

In contrast, the monodentate nitrito complex (TCB)Ru(κ¹-ONO), which is likewise see-saw in the neutral species (Fig. 6a), undergoes a geometry change upon reduction yielding a structure where the nitrito becomes κ^2 -N-O (Fig. 6b). Notably, upon reduction the internal N-O distance lengthens by 0.11 Å and the terminal N-O distance increases by 0.06 Å (see Fig. S31† for full bond length analysis). Moreover, the pendent oxygen does not lie on the Ru-O-N plane, a feature unknown in MNO2 chemistry. This facilitates back donation into the N-O π -system, where the spin density plot shows population of the nitrito π^* (Fig. 6c). This is corroborated by the bond length changes and shifts in N-O stretching frequencies (Fig. S31†). For more insight into the deviation from coplanarity of the [RuON] fragment and the terminal oxygen, analysis of several crystallographically characterized M-RNO complexes was done. This data is summarized in Table S9,† with the conclusion that nonplanarity between the [MNO] fragment and R is indicative of reduction of the RNO unit to [RNO]. This deviation from planarity is also accompanied by a significant lengthening of the N-O bond. All of these data point toward a similar phenomenon in [(TCB)Ru(ONO)], where the nitrite ligand is best described as κ^2 and reduced by one electron. Overall, these monodentate nitrite calculations indicate that O-bound nitrito can act as a π -acid in this TCB system, but does so by becoming κ^2 .

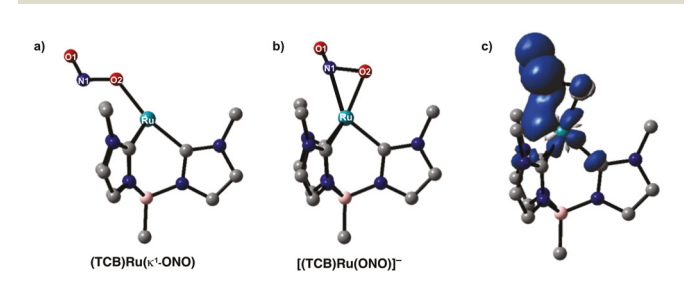


Fig. 6 (a) Optimized structure for (TCB)Ru(κ¹-ONO) (b) optimized structure for [(TCB)Ru(ONO)] and (c) spin density plot (0.002 au) of [(TCB)Ru(ONO)]-.

It is important to note that the initial test suite of Ru and Rh complexes (Fig. 2 and ESI†) were also attempted with bidentate nitrate as the starting geometry, but all geometry optimizations yield structures with monodentate nitrate. This is due to geometric and electronic preferences of this initial suite of compounds compared to the C_{3y} enforcing TCB ligand, and is something that should be taken into account in design of these types of compounds for N-O bond weakening.

The effect of six coordinate metal. The calculations thus far show significant promise for N-O bond weakening, even in unsaturated complexes. Therefore, we hypothesized that 18 valence electron species will more forcefully direct added electrons to nitrate. We first evaluated this by adding a Lewis base (NH₃) to the open coordination site of the 16 valence electron square pyramidal (TCB)Ru(κ^2 -NO₃).

For the neutral species, (TCB)Ru(κ^2 -NO₃)(NH₃), the octahedral complex maintains truly bidentate nitrate on geometry optimization (Fig. 7a). Upon reduction to $[(TCB)Ru(\kappa^2-NO_3)]$ (NH₃)] (Fig. 7b) the bond length changes are consistent with population of the nitrate π^* . Additionally, the stretching frequencies are reduced by 268 and 354 cm⁻¹ and the spin density plot (Fig. 7c) shows complete localization on nitrate with no metal character. Compared to the five coordinate $[(TCB)Ru(\kappa^2-NO_3)]^-$, this six coordinate $[(TCB)Ru(\kappa^2-NO_3)]$ (NH₃)] shows that the nitrate is further pyramidalized, with a Ru-N1-O1 angle of 137.7°.

We also considered a competitive π -acid to fill the sixth coordination site: CO. The optimized structures for (TCB)Ru $(\kappa^2\text{-NO}_3)(\text{CO})$ and $([\text{TCB}]\text{Ru}(\kappa^2\text{-NO}_3)(\text{CO})]^-$ (Fig. 7d and e) notably show no pyramidalization of the nitrate. The unpaired spin of [(TCB)Ru(κ²-NO₃)(CO)] occupies a ruthenium d-orbital back donating into the CO π^* (Fig. 7f), which is accompanied

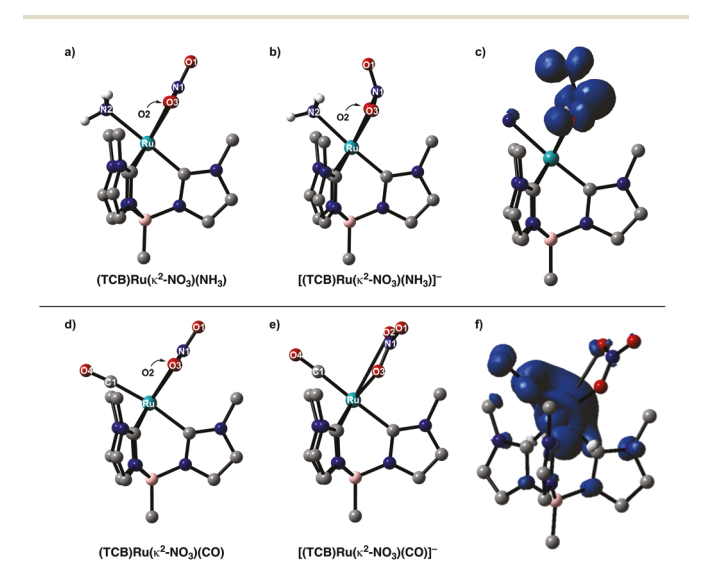


Fig. 7 (a) Optimized structure for (TCB)Ru(κ^2 -NO₃)(NH₃) (b) optimized structure for $[(TCB)Ru(\kappa^2-NO_3)(NH_3)]^-$ (c) spin density plot (0.002 au) of $[(TCB)Ru(\kappa^2-NO_3)(NH_3)]^-$ (d) optimized structure for $(TCB)Ru(\kappa^2-NO_3)$ (CO) (e) optimized structure for $[(TCB)Ru(\kappa^2-NO_3)(CO)]^-$ and (f) spin density plot (0.002 au) of $[(TCB)Ru(\kappa^2-NO_3)(CO)]^{-}$.

Dalton Transactions Paper

by a breaking of the Ru-O2 bond (lengthened by 0.96 Å). Therefore, the addition of a π -acidic carbonyl ligand to (TCB) $Ru(\kappa^2-NO_3)$ effectively eclipses the π -acidity of nitrate, which becomes monodentate. This is due to the π^* orbital of CO lying lower than that of nitrate. Overall, this shows that incorporation of CO leads to undesirable competition for back donation.

Tris-pyrazolyl borate (Tp) analogs: the influence of ancillary ligands on back donation to nitrate, nitrito and nitro

Nitrate. Because this work seeks predictive design principles for complexes that can weaken N-O bonds, we were interested in probing how central this tris NHC ligand is to the nitrate reduction described above. We therefore considered a weaker tris-pyrazolyl borate donor (Tp, Fig. 3c) for comparison to the five- and six-coordinate TCB cases described above. Geometry optimization of the 16-valence electron species (Tp)Ru(κ^2 -NO₃) (Fig. 8a) yields a square pyramidal structure similar to (TCB) $Ru(\kappa^2-NO_3)$ however each Ru-O distance is shortened by 0.076 Å compared to the TCB complex, showing the influence of the strongly donating carbenes. The unpaired spin in the reduced $[(Tp)Ru(\kappa^2-NO_3)]^-$ (Fig. 8b) is primarily a ruthenium d-orbital, which is directed towards the vacant site of the square pyramid (Fig. 8c). This follows the generality that d⁶ is square pyramidal and d⁷ is the same, with its SOMO in the open coordination site. The spin density plot also shows only minor nitrate contribution, and the bond length changes as well as the N-O stretching frequencies (Fig. S36†) are not consistent with back donation into the π -system of nitrate upon reduction. The lack of nitrate reduction observed with Tp compared to an otherwise identical TCB system arises from the transition from strongly σ-donating TCB to weaker Tp; an orbital inversion causes the ruthenium d₂₂ orbital energy to drop below the energy of the NO_3^- ligand π^* orbital (Fig. 8d).

These results led us to consider the 6-coordinate option: will a saturated system facilitate back donation, even with a weaker Tp donor? We probed this by geometry optimizing (Tp) $Ru(\kappa^2-NO_3)(NH_3)$ (Fig. 8e) and the one-electron reduced [(Tp) $Ru(\kappa^2-NO_3)(NH_3)$]⁻ (Fig. 8f). The neutral (Tp)Ru(κ^2-NO_3)(NH₃) optimizes to an octahedral structure, similar to that of (TCB) $Ru(\kappa^2-NO_3)(NH_3)$. Addition of an extra electron to form [(Tp)Ru $(\kappa^2\text{-NO}_3)(\text{NH}_3)$ shows exclusive population of the nitrate π^* (Fig. 8g) analogous to what was observed in the TCB case. Additionally, the nitrate is pyramidalized, with a Ru-N1-O1 angle of 137.7°, identical to that of $[(TCB)Ru(\kappa^2-NO_3)(NH_3)]^-$. The -NH3 binding yields an 18 valence electron neutral complex, which favors nitrate reduction instead of metal reduction to give 19 valence electron ruthenium. The structural parameters as well as the stretching frequencies for [(Tp) $Ru(\kappa^2-NO_3)(NH_3)$ are similar to $[(TCB)Ru(\kappa^2-NO_3)(NH_3)]$ and are detailed in the ESI.†

Nitrite. For comparison, calculations were also done on (Tp) $Ru(\kappa^2$ -ONO) and $[(Tp)Ru(\kappa^2$ -ONO)]⁻. Once again, the bidentate nitrite complex is square pyramidal about ruthenium (Fig. S37a†). The spin density of monoanionic $[(Tp)Ru(\kappa^2 -$ ONO)] is mainly located in a metal orbital, directed toward the vacant site of the square pyramid (Fig. S37b†). All bond length changes and frequency shifts are modest compared to those seen for the TCB analogue (Fig. S37c†). This result is analogous to the nitrate results with weaker Tp donor; orbital inversion upon changing from TCB to Tp inhibits nitrite reduction.

Invoking full N-O bond cleavage: addition of a proton

To this point we have been analyzing the electron transfer part of proton coupled electron transfer. The evidence presented above shows that it is possible to achieve reduced NO₃²⁻ coordinated to ruthenium. We were therefore curious if protona-

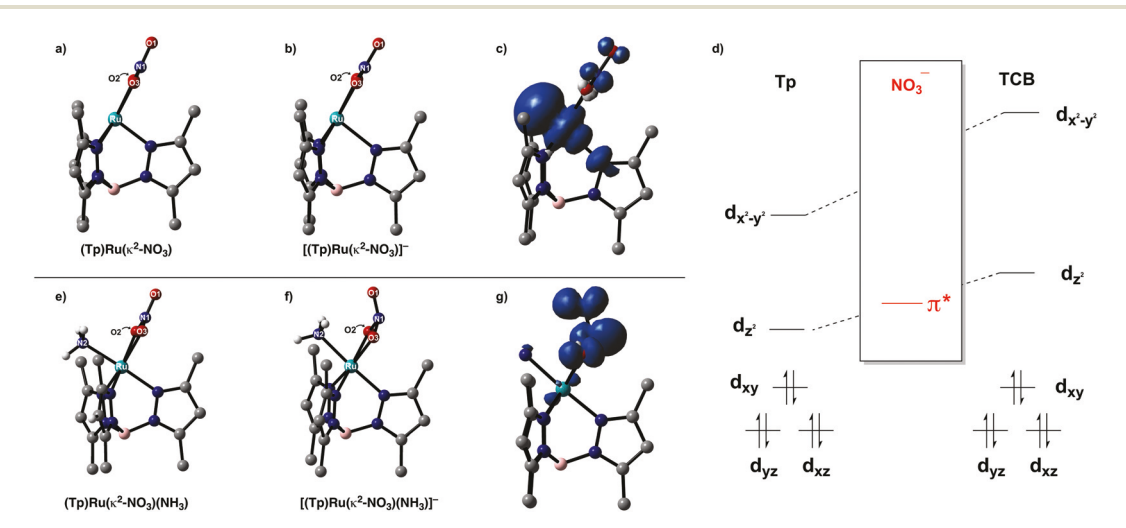


Fig. 8 (a) Optimized structure for $(Tp)Ru(\kappa^2-NO_3)$ (b) optimized structure for $[(Tp)Ru(\kappa^2-NO_3)]^-$ (c) spin density plot (0.002 au) of $[(Tp)Ru(\kappa^2-NO_3)]^-$ (d) qualitative MO diagrams for square pyramidal splitting with Tp and TCB, showing relavent general energies compared to the nitrate π^* (e) optimized structure for (Tp)Ru(κ^2 -NO₃)(NH₃) (f) optimized structure for [(Tp)Ru(κ^2 -NO₃)(NH₃)]⁻ (g) spin density plot (0.002 au) of [(Tp)Ru(κ^2 -NO₃) $(NH_3)]^-$.

tion would trigger N-O bond cleavage, as there are several reported examples of the importance of protonation in NO_x reduction. 25,27,33-38

Protonation of $[(TCB)Ru(\kappa^2-NO_3)]^{0/-}$. We considered protonation of neutral (TCB)Ru(κ²-NO₃) at both the terminal and internal oxygens, which yields isomers [(TCB)Ru(κ^2 -NO₃H)]⁺ (Fig. 9a and b) that differ by only 0.4 kcal mol⁻¹, slightly favouring the terminal OH. All gas phase protonations were extremely exergonic; therefore, we explored solvent corrections with varied dielectric constants for increased experimental relevance (see ESI† for more details on solvent corrections). The reported thermodynamic data is for corrections using acetonitrile solvent, but we also considered THF and benzene. As a general trend, the reactions in Scheme 1 are more exergonic as the dielectric constant decreases, with a more exacerbated difference in favorability amongst the various solvents for reactions c and d (Scheme 1). Both protonations cause a distortion from bidentate nitrate so that one Ru-O distance lengthens significantly and the N-O distance of the protonated oxygen increases (Fig. 9a and b). Looking at the overall thermodynamics of protonation of the neutral species, the process is favourable by 8.4 kcal mol⁻¹, but no N-O bond scission is observed (Scheme 1a). We were therefore interested in protonation of the pre-reduced species, $[(TCB)Ru(\kappa^2-NO_3)]^-$. We again considered protonation at the both the internal and terminal oxygens (optimized structures shown in Fig. 9c and d), finding both processes to be very exergonic (Scheme 1c and d).

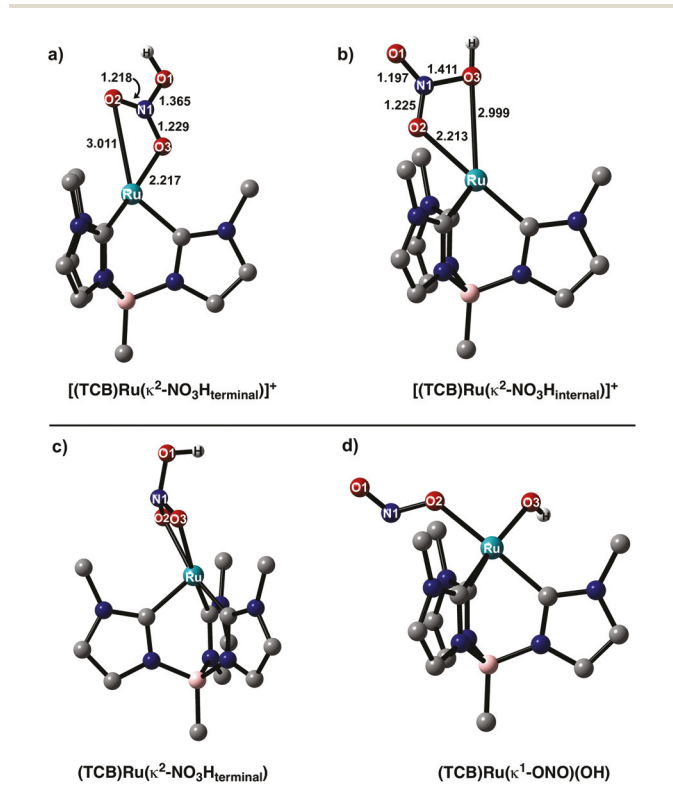
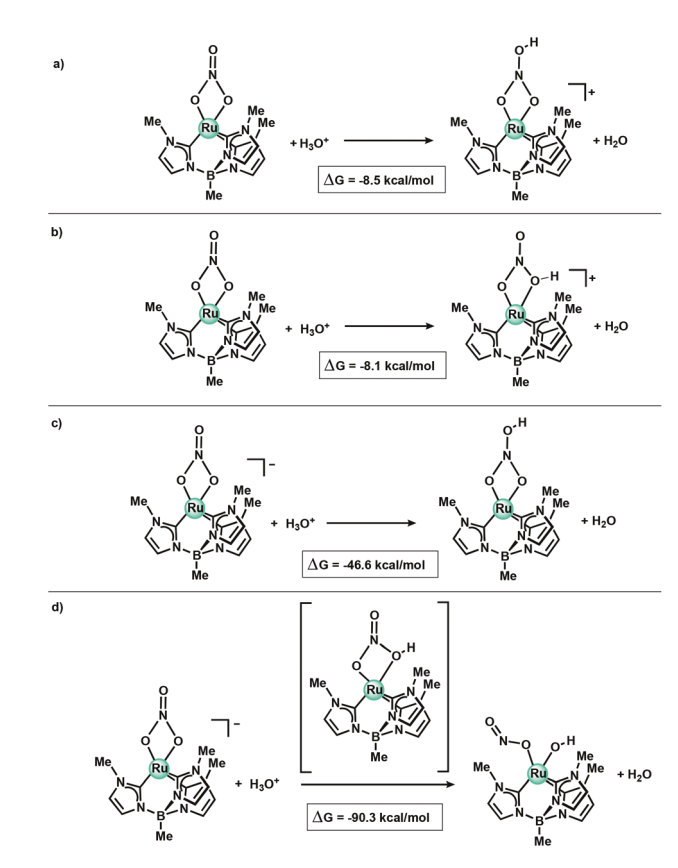


Fig. 9 Optimized structure and selected bond lengths for (a) [(TCB)Ru $(\kappa^2\text{-NO}_3H_{terminal})]^+ \quad \text{(b)} \quad [(TCB)Ru(\kappa^2\text{-NO}_3H_{internall})]^+ \quad \text{(c)} \quad (TCB)Ru(\kappa^2\text{-NO}_3H_{internall})]^+$ $NO_3H_{terminal}$) and (d) (TCB)Ru(κ^1 -ONO)(OH).



Scheme 1 Thermodynamics for protonation of (a) (TCB)Ru(κ^2 -NO₃) at the terminal oxygen (b) $(TCB)Ru(\kappa^2-NO_{\tau})$ at the internal oxygen (c) $[(TCB)Ru(\kappa^2-NO_3)]^-$ at the terminal oxygen and (d) $[(TCB)Ru(\kappa^2-NO_3)]^-$ at the internal oxygen.

Protonation of the internal position is more favorable by 43.7 kcal mol⁻¹, and gives a product that leads to spontaneous (essentially barrierless) cleavage of an N-O bond to form the 5-coordinate species (TCB)Ru((κ^1 -ONO)(OH) (Fig. 9d). This redox event is the source of its greater stability. Intramolecular redox that leads to N-O bond cleavage to form this Ru^{III} product is possible due to the initially threefold connectivity of that oxygen, representing a two-electron reduction of nitrate from only a single added electron because the second electron is furnished from Ru^{II}. The assignment of Ru^{III} is supported by both a spin density plot and corresponding orbital diagram (Fig. S32†) of (TCB)Ru((κ^1 -ONO)(OH). The spin density plot shows spin density primarily localized on ruthenium, and the SOMO of the corresponding orbital diagram is the d_{xy} orbital, which is consistent with a 1-electron oxidation of RuII from the qualitative MO diagram in Fig. 8d.

The thermodynamics of each reaction show that the O-protonation of reduced $[(TCB)Ru(\kappa^2-NO_3)]^-$ is highly exergonic which reflects the large amount of electron density on the NO₃²⁻. Many deoxygenations of nitrate are two electron processes but liberation of the nitrogen radical NO2 is a one-electron deoxygenation alternative where oxide stays with the metal and NO2 is liberated. While this has been observed experimentally with very oxophilic cerium, 39,40 the present

exploration of coordinated nitrate has not encountered that process.

Dalton Transactions

When H⁺ is exchanged for Na⁺ (stabilized by a coordinated dimethoxyethane solvent molecule), no spontaneous N–O bond scission is observed; however, there is evidence for electrophilically induced N–O bond weakening at the electron rich dianionic nitrate radical, where Na⁺ binds two nitrate oxygens (see ESI[†] for full discussion on addition of Na⁺).

The four reactions in Scheme 1 were also performed with Tp, which follows the same thermodynamic and structural trends as TCB, including N–O bond scission upon internal oxygen protonation of $[(Tp)Ru(\kappa^2-NO_3)]^-$ (see ESI† for full details).

Protonation of $[(TCB)Ru(\kappa^2-ONO)]^{0/-}$ and $[(TCB)Ru(NO_2)]^{0/-}$. Analogous calculations were done on both the protonated bidentate O-bound nitrite and N-bound nitrite [(TCB)Ru] complexes in order to determine if the same N-O bond cleavage would be observed when the nitrogen is in the +3 oxidation state. Notably, O-protonation of neutral (TCB)Ru(κ²-ONO) to form [(TCB)Ru(ONOH)]⁺ (Fig. S33†) causes bidentate nitrite to become essentially monodentate, with the protonated Ru-O distance elongating by 0.54 Å. To compensate for the lost donation from the protonated oxygen, the other Ru-O distance shortens by 0.10 Å. The N-OH bond is lengthened by 0.14 Å, consistent with the loss of double bond character. In contrast, protonation of the pre-reduced $[(TCB)Ru(\kappa^2-ONO)]^-$ results in barrieless N-O bond scission, analogous to the reactivity described with nitrate above, and forms (TCB)Ru(OH)(ON) where the formation of an isonitrosyl is not an impediment to bond cleavage. A full description of these calculations is available in the ESI.†

How do things differ for Fe vs. Ru?

Having identified the nitrate dianion in $[(TCB)Ru(\kappa^2-NO_3)]^-$, we wanted to ensure that the spin density on nitrate was not simply a result of the unfavorability of generating the unusual oxidation state Ru^I. We therefore turned to comparative calculations on Fe, due to the possibility of a more attainable Fe^I oxidation state upon reduction. (TCB)Fe(κ^2 -NO₃) and [(TCB)Fe (κ^2-NO_3) were optimized at all three possible spin states. For neutral (TCB)Fe(κ^2 -NO₃), all three spin states are essentially isoenergetic, with the quintet lowest, triplet +3.4 kcal mol⁻¹ and the singlet only 0.4 kcal mol⁻¹ above the quintet. The fact that each spin state is so close in energy suggests that all three are available for reduction. Structurally, the singlet has truly bidentate nitrate (Fig. 10a), with equidistant Fe-O distances. With population of Fe-O antibonding orbitals in the triplet and quintet spin states, one Fe-O distance lengthens as a result of no empty orbital available for donation from the pendant oxygen (Fig. 10b and c). Upon reduction to [(TCB)Fe (κ^2-NO_3)]⁻, the doublet is lowest in energy, followed by the quartet (+3.6 kcal mol⁻¹) and then the sextet (+15.8 kcal mol⁻¹). We therefore focused on the doublet and quartet spin states (optimized structures shown in Fig. 10d and e). The doublet resembles $[(TCB)Ru(\kappa^2-NO_3)]^-$, with a pyramidal nitrate nitrogen, significant spin density in nitrate π^* (Fig. 10f), and bond lengths and stretching frequencies con-

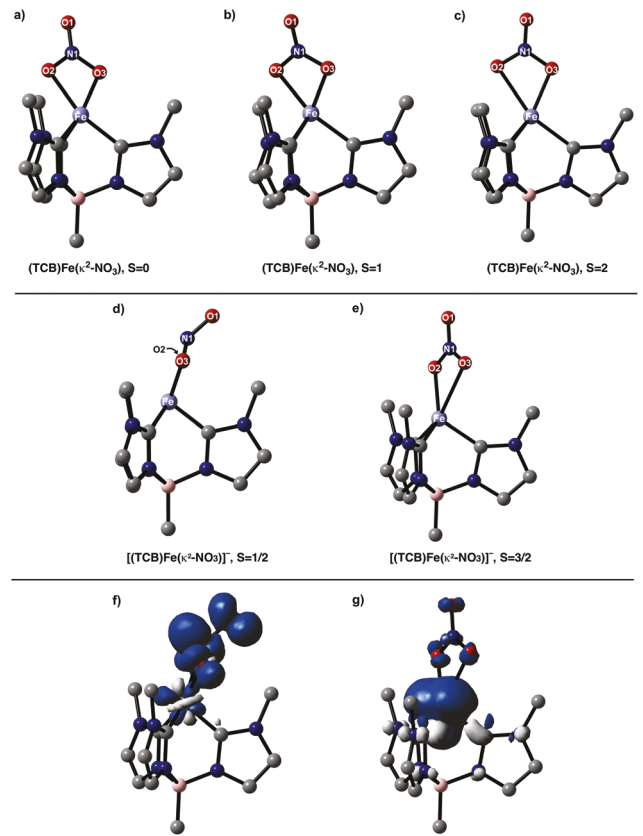


Fig. 10 Optimized structure for (a) (TCB)Fe(κ^2 -NO₃), S=0 (b) (TCB)Fe (κ^2 -NO₃), S=1 (c) (TCB)Fe(κ^2 -NO₃), S=2 (d) [(TCB)Fe(κ^2 -NO₃)]⁻, S=1/2 (e) [(TCB)Fe(κ^2 -NO₃)]⁻, S=3/2 (f) spin density plot (0.002 au) for [(TCB)Fe(κ^2 -NO₃)]⁻, S=1/2 (g) spin density plot (0.002 au) for [(TCB)Fe(κ^2 -NO₃)]⁻, S=3/2.

sistent with population of the nitrate π^* -system. In contrast, the charge density for the quartet is mostly localized on iron (Fig. 10g), with only a small amount of nitrate participation. Similar to the neutral species, the higher spin and population of more antibonding orbitals in quartet [(TCB)Fe(κ^2 -NO₃)]⁻ causes significant elongation of one Fe–O distance. Although several spin states for both (TCB)Fe(κ^2 -NO₃) and [(TCB)Fe(κ^2 -NO₃)]⁻ are close in energy, the significant spin density on nitrate of doublet [(TCB)Fe(κ^2 -NO₃)]⁻ shows that ruthenium is not the only metal for achieving N–O bond weakening.

Conclusions

In summary, this work helps to outline design principles that either help or hinder electron donation into the π^* system of nitrogen oxyanions. The use of a strongly donating triscarbene borate ligand, accompanied by bidentate oxyanion binding successfully facilitates charge accumulation in reduced nitrate and nitrite complexes. Coordinative and electronic saturation also encourage population of nitrate π^* upon reduction, even with the weaker trispyrazolyl borate donor. The incorporation of ancillary ligands with low lying π^* systems, such as CO or

pyridine, is shown to be unproductive, as these ligands act as competitors for charge density upon reduction. Bond length changes, infrared stretching frequencies, and pyramidalization of nitrogen in coordinated NO_x species are all indicators of increased electron density within the oxyanion units. With increased charge on the nitrogen oxyanions in the [(TCB)Ru $(\kappa^2\text{-NO}_3)$]⁻, $[(\text{TCB})\text{Ru}(\kappa^2\text{-ONO})]$ ⁻, and $[(\text{TCB})\text{Ru}(\text{NO}_2)]$ ⁻ complexes, protonation yields essentially barrierless N-O bond cleavage to give either hydroxide and nitrosyl ligands or hydroxide and isonitrosyl ligands. While the addition of Na⁺ as an electrophile does not invoke N-O bond cleavage, there is evidence for electrophile assisted N-O bond weakening. Lastly, while the d orbital energies of ruthenium may be less negative in energy than its 3d counterpart, we show that charge transfer to NO₃⁻ is possible with iron upon reduction of singlet (TCB) $Fe(\kappa^2-NO_3)$ to doublet $[(TCB)Fe(\kappa^2-NO_3)]^-$ (where the doublet is the lowest energy spin state). This work builds on the growing body of work regarding homogenous NO_x reduction and provides new insight into tangible experimental parameters that can be used to encourage N-O bond scission.

Conflicts of interest

There are no conflicts to declare.

Acknowledgements

This work was supported by the Indiana University Office of Vice President for Research and the National Science Foundation by grant CHE-1362127. This research was supported in part by Lilly Endowment, Inc., through its support for the Indiana University Pervasive Technology Institute.

References

- 1 W. K. Dodds, W. W. Bouska, J. L. Eitzmann, T. J. Pilger, K. L. Pitts, A. J. Riley, J. T. Schloesser and D. J. Thornbrugh, Environ. Sci. Technol., 2009, 43, 12-19.
- 2 R. J. Diaz and R. Rosenberg, Science, 2008, 321, 926.
- 3 J. G. Morris, Annu. Rev. Environ. Resour., 1999, 24, 367-390.
- 4 S. Matassa, D. J. Batstone, T. Hülsen, J. Schnoor and W. Verstraete, Environ. Sci. Technol., 2015, 49, 5247-5254.
- 5 J. N. Galloway, J. D. Aber, J. W. Erisman, S. P. Seitzinger, R. W. Howarth, E. B. Cowling and B. J. Cosby, BioScience, 2003, 53, 341-356.
- 6 D. Fowler, M. Coyle, U. Skiba, M. A. Sutton, J. N. Cape, S. Reis, L. J. Sheppard, A. Jenkins, B. Grizzetti, J. N. Galloway, P. Vitousek, A. Leach, A. F. Bouwman, K. Butterbach-Bahl, F. Dentener, D. Stevenson, M. Amann and M. Voss, Philos. Trans. R. Soc., B, 2013, 368, 20130164.
- 7 M. Sebilo, B. Mayer, B. Nicolardot, G. Pinay and A. Mariotti, Proc. Natl. Acad. Sci. U. S. A., 2013, 110, 18185-18189.
- 8 R. Vaquer-Sunyer and C. M. Duarte, Proc. Natl. Acad. Sci. U. S. A., 2008, 105, 15452-15457.

- 9 L. W. Canter, Nitrate in Groundwater, Lewis Publishers, Boca Raton, 1997.
- 10 S. Xu, D. C. Ashley, H.-Y. Kwon, G. R. Ware, C.-H. Chen, Y. Losovyj, X. Gao, E. Jakubikova and J. M. Smith, Chem. Sci., 2018, 9, 4950-4958.
- 11 S. E. Braley, D. C. Ashley, E. Jakubikova and J. M. Smith, Chem. Commun., 2020, 56, 603-606.
- 12 G.-F. Chen, Y. Yuan, H. Jiang, S.-Y. Ren, L.-X. Ding, L. Ma, T. Wu, J. Lu and H. Wang, Nat. Energy, 2020, 5, 605-613.
- 13 T. Chen, H. Li, H. Ma and M. T. M. Koper, Langmuir, 2015, 31, 3277-3281.
- 14 J. Choi, H.-L. Du, C. K. Nguyen, B. H. R. Suryanto, A. N. Simonov and D. R. MacFarlane, ACS Energy Lett., 2020, 5, 2095-2097.
- 15 M. Duca and M. T. M. Koper, Energy Environ. Sci., 2012, 5, 9726-9742.
- 16 Y. Wang, W. Zhou, R. Jia, Y. Yu and B. Zhang, Angew. Chem., Int. Ed., 2020, 59, 5350-5354.
- 17 S. Challagulla, K. Tarafder, R. Ganesan and S. Roy, J. Phys. Chem. C, 2017, 121, 27406-27416.
- 18 Z. Geng, Z. Chen, Z. Li, X. Qi, X. Yang, W. Fan, Y. Guo, L. Zhang and M. Huo, Dalton Trans., 2018, 47, 11104-11112.
- 19 N. Krasae and K. Wantala, Appl. Surf. Sci., 2016, 380, 309-
- 20 S. Tawkaew, Y. Fujishiro, S. Yin and T. Sato, Colloids Surf., A, 2001, 179, 139-144.
- 21 M. Yamauchi, R. Abe, T. Tsukuda, K. Kato and M. Takata, J. Am. Chem. Soc., 2011, 133, 1150-1152.
- 22 J. Seo, A. C. Cabelof, C.-H. Chen and K. G. Caulton, Chem. Sci., 2019, 10, 475-479.
- 23 D. M. Beagan, V. Carta and K. G. Caulton, Dalton Trans., 2020, 49, 1681-1687.
- 24 C. L. Ford, Y. J. Park, E. M. Matson, Z. Gordon and A. R. Fout, Science, 2016, 354, 741.
- 25 M. Delgado and J. D. Gilbertson, Chem. Commun., 2017, 53, 11249-11252.
- 26 C. Uyeda and J. C. Peters, J. Am. Chem. Soc., 2013, 135, 12023-12031.
- 27 C. M. Moore and N. K. Szymczak, Chem. Sci., 2015, 6, 3373-
- 28 J. J. Scepaniak, C. S. Vogel, M. M. Khusniyarov, F. W. Heinemann, K. Meyer and J. M. Smith, Science, 2011, 331, 1049-1052.
- 29 M. K. Goetz, E. A. Hill, A. S. Filatov and J. S. Anderson, J. Am. Chem. Soc., 2018, 140, 13176-13180.
- 30 J. M. Smith, D. E. Mayberry, C. G. Margarit, J. Sutter, H. Wang, K. Meyer and R. P. Bontchev, J. Am. Chem. Soc., 2012, 134, 6516-6519.
- 31 R. A. Juarez, W.-T. Lee, J. M. Smith and H. Wang, Dalton Trans., 2014, 43, 14689-14695.
- 32 A. R. Cook, N. Dimitrijevic, B. W. Dreyfus, D. Meisel, L. A. Curtiss and D. M. Camaioni, J. Phys. Chem. A, 2001, **105**, 3658-3666.
- 33 S. Xu, H.-Y. Kwon, D. C. Ashley, C.-H. Chen, E. Jakubikova and J. M. Smith, Inorg. Chem., 2019, 58, 9443-9451.

Dalton Transactions Paper

- 34 A. C. Cabelof, V. Carta, C.-H. Chen and K. G. Caulton, *Dalton Trans.*, 2020, **49**, 7891–7896.
- 35 P. M. Cheung, K. T. Burns, Y. M. Kwon, M. Y. Deshaye, K. J. Aguayo, V. F. Oswald, T. Seda, L. N. Zakharov, T. Kowalczyk and J. D. Gilbertson, J. Am. Chem. Soc., 2018, 140, 17040–17050.
- 36 Y. M. Kwon, M. Delgado, L. N. Zakharov, T. Seda and J. D. Gilbertson, *Chem. Commun.*, 2016, 52, 11016–11019.
- 37 X. Qin, L. Deng, C. Hu, L. Li and X. Chen, *Chem. Eur. J.*, 2017, 23, 14900–14910.
- 38 C.-C. Tsou, W.-L. Yang and W.-F. Liaw, *J. Am. Chem. Soc.*, 2013, 135, 18758–18761.
- 39 P. L. Damon, G. Wu, N. Kaltsoyannis and T. W. Hayton, J. Am. Chem. Soc., 2016, 138, 12743–12746.
- 40 M. K. Assefa, G. Wu and T. W. Hayton, *Chem. Sci.*, 2017, 8, 7873–7878.